Large Tunable Thermoelectric Effects in Superconducting Spin Valves with Commercially Available Materials

Pablo Tuero,[1,*] Johanne Bratland Tjernshaugen,[2,*] Carlos Sanchez,[1] César Gonzalez-Ruano,[1,3] Yuan Lu,[4] Jacob Linder,[2,†] and Farkhad G. Aliev[5,‡]

[1] *Departamento Física de la Materia Condensada C-III, Universidad Autónoma de Madrid, 28049 Madrid, Spain*
[2] *Center for Quantum Spintronics, Department of Physics, Norwegian University of Science and Technology, NO-7491 Trondheim, Norway*
[3] *Department of Electrical Engineering, School of Engineering (ICAI) and Institute for Research and Technology (IIT), Universidad Pontificia Comillas, Alberto Aguilera 23, 28015 Madrid, Spain*
[4] *Université de Lorraine, CNRS, Institut Jean Lamour, F-54000 Nancy, France*
[5] *Departamento Física de la Materia Condensada C-III, Instituto Nicolás Cabrera (INC) and Condensed Matter Physics Institute (IFIMAC), Universidad Autónoma de Madrid, 28049 Madrid, Spain*

(Received 24 January 2025; revised 14 May 2025; accepted 25 June 2025; published 16 July 2025)

Recent studies have revealed magnetically controllable thermoelectric effects in superconductor/ferromagnet (S/F) structures. A tunable cryogenic thermoelectric generator needs not only a high conversion factor between electricity and heat, but also a large change in the thermoelectric output when switching the magnetic state of the device. However, the reported modifications in thermoelectric power are either minimal, involve superconductors with relatively low critical temperatures (below 1 K), or do not utilize commercially available spintronic materials. Here, we experimentally measure and numerically model thermoelectric effects in fully epitaxial ferromagnet/superconductor/ferromagnet (F/S/F) junctions based on commercially available easily grown materials, as well as their dependence on the magnetic configuration of the ferromagnetic (F) electrodes. We observe sizeable Seebeck coefficients for the parallel alignment of the F electrodes, reaching values of about 100 μV/K. Importantly, we find a decrease of the thermoelectric signal of more than an order of magnitude when switching from a parallel to an antiparallel configuration, constituting a large thermoelectric spin-valve effect. Theoretical modeling based on a self-consistent nonequilibrium Keldysh-Usadel Green's function theory, combined with micromagnetic simulations, qualitatively reproduce the experimental findings. The thermoelectric effect is optimized when there is a large spin-dependent electron-hole asymmetry in the superconductor combined with spin-dependent transmission through the interfaces. These findings pave the way for the development of efficient and versatile cryogenic thermoelectric heat engines.

DOI: 10.1103/xbgg-gttc

I. INTRODUCTION

The conversion of heat into electricity and vice versa is known as thermoelectricity [1,2]. This field of research has received increasing attention over recent decades, not only for the purpose of gaining insight into the fundamental physics of new materials [3,4] but also due to the large number of industrial applications that thermoelectricity enables. These include vastly different areas such as temperature control (cooling) of electronic devices, air conditioning, food refrigeration, and ultrasensitive detection of electromagnetic radiation [5–9].

A prominent challenge with thermoelectricity occurs in the low-temperature regime. Whereas conventional thermoelectric materials typically operate in the (100–400)-K regime, their performance, in terms of, e.g., the Seebeck coefficient, drastically drops at lower temperatures [10]. Therefore, there exists a need to design better material platforms that can yield efficient thermoelectricity even under cryogenic conditions. One promising application of thermoelectricity under cryogenic conditions is localized cryogenic cooling. This can be achieved using either thermoelectric materials that are highly efficient at low temperatures [11] or superconductor-based microscale refrigerators [12], which would complement the existing liquid nitrogen, helium, or magnetic salt cooling procedures.

*These authors contributed equally to this work.
†Contact author: jacob.linder@ntnu.no
‡Contact author: farkhad.aliev@uam.es

Superconductors are excellent thermoelectric materials when combined with ferromagnets [2,13]. This emergent phenomenon has been predicted more than a decade ago [14,15] and subsequently experimentally confirmed [16]. The key mechanism behind this emergent thermoelectricity is a spin-dependent particle-hole asymmetry in a superconductor that coexists with a spin-splitting field, which in turn is utilized by using the spin-selective transport properties of ferromagnets. Combining superconductors with antiferromagnets also produces enhanced thermoelectric effects [17]. Moreover, large thermoelectric effects have been predicted [18] and experimentally confirmed [19] in tunnel junctions with two different superconductors in the nonlinear regime, due to spontaneous breaking of electron-hole symmetry.

The investigation of heat dissipation and energy harvesting in superconductor/ferromagnet (S/F) hybrids and in quantum devices in general [20] is an important area of research. For example, quantum error-correction operations produce heating [21], potentially harvestable by low-temperature Peltier elements. In that context, obtaining the maximum possible Seebeck coefficients at the lowest possible temperatures (where actual quantum computers operate) and with minimum possible temperature gradients, could be important for the potential applications of magnetic-state-controlled thermoelectricity. Magnetic control over thermoelectric effects could improve localized cooling for quantum devices, such as superconducting qubits and ultrasensitive detectors [22] by dynamically tuning heat flow. Magnetically controlled thermoelectric transport could also be used to manipulate heat flux (thermal diodes) [23], in a way analogous to how electronics manipulate electric energy. Last but not least, the above-mentioned waste heat from superconducting or other low-temperature electronic systems could be converted into usable electrical energy via magnetically tunable thermoelectric generators [13,24].

Very recently, it has been predicted [25] and experimentally demonstrated [24,26] that interfacing a superconductor with two ferromagnets allows the Seebeck coefficient of the system to be tuned via the magnetic alignment of the ferromagnetic regions. However, in order for such an effect to be viable for cryogenic thermoelectric applications, a number of conditions have to be met. First, one would need to use commercially available materials with high spin polarization, which are easily grown. Second, the resulting magnitude of the thermoelectric effect would need to be sizeable at temperatures well below T_c and there should be a large difference in the Seebeck coefficient for the parallel (P) and antiparallel (AP) magnetic states of the spin valve.

In this work, we report the experimental observation of a large superconducting thermoelectric spin-valve effect that meets all of the key criteria stated above. This represents a major advance compared to previous works on related S/F structures [24,26]. Specifically, we study the spin-dependent transport and thermoelectric response in Fe/MgO/V/MgO/Fe/Co structures as a function of the relative alignment between the soft (Fe) and hard (Fe/Co) ferromagnetic (F) electrodes. An important reason to use vanadium in our Fe/MgO/V-based junctions is its nearly perfect crystalline structure matching with Fe and MgO, allowing the superconductor to be grown on top of an almost fully spin-polarized (Fe/MgO) ferromagnet with an effective spin polarization exceeding 80%. Our findings demonstrate a large thermoelectric effect, with a Seebeck coefficient exceeding 100 μV/K at base temperatures around $0.1T_c$, where T_c is the critical temperature of the V film. Importantly, we report a large change in the thermoelectric response—greater than a factor of 10—when switching the device from the antiparallel (AP) to the parallel (P) alignment of the electrodes. Analyzing the results, we find a high sensitivity of the thermoelectric response to magnetic domain rotation and motion, as highlighted by the comparison of experimental thermoelectric and magnetoresistance data with micromagnetic simulations and theoretical modeling based on the nonequilibrium Keldysh-Usadel Green's function formalism.

II. EXPERIMENTAL RESULTS

In Fig. 1(a), we illustrate the experimental setup and the specific junctions under study. We measure magnetoresistance (MR) and thermoelectric (TE) effects in epitaxial Fe(45)/MgO(2.3)/V(40)/MgO(2.3)/Fe(10)/Co(20) junctions grown on MgO(001) substrates, with layer thicknesses provided in nanometers. Further details on the junction growth, characterization, experimental setup, and simulation procedures are available in the Supplemental Material [27]. In these F1/S/F2 junctions, V is the Bardeen-Cooper-Schrieffer (BCS) superconductor (S), Fe serves as the soft magnetic electrode (F1), and Fe/Co functions as the magnetically hard electrode (F2), while the MgO acts as a symmetry-filtering tunnel barrier, facilitating high spin polarization (p) in Fe, exceeding 0.7–0.8 [28,29]. Due to the weak antiferromagnetic coupling of the junctions [30–33], two distinct magnetic states are experimentally observed: at low fields, the junctions tend toward an antiparallel alignment, while a moderate external magnetic field (H) of 0.1–0.2 T will drive them into a parallel magnetic state. In Fig. 1(b), we provide a low-bias electron-transport characterization of the junctions in the superconducting state for both magnetic alignments. The oscillations in the conductance curves are likely due to McMillan resonances [33,34] that may occur for clean samples. In Fig. 1(c), we provide temperature-dependent subgap conductance measurements that show a superconducting critical temperature of $T_c = 4.7$ K, marked by an abrupt change of slope. This value is close to that expected from the dependence of T_c on the thickness for vanadium

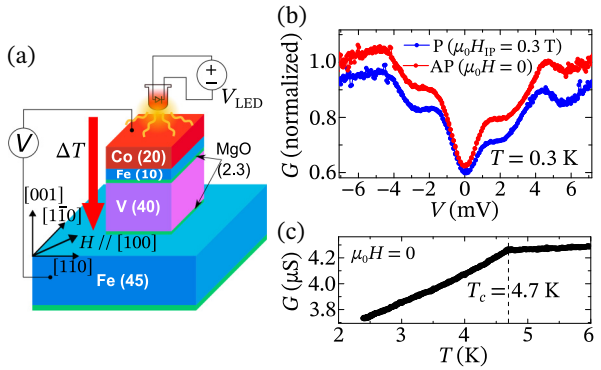

FIG. 1. (a) A sketch of the ferromagnet/superconductor/ferromagnet (F/S/F) junctions when heated by a light-emitting diode (LED). The black arrows show the crystalline axes and the direction of the applied magnetic field. The layer thicknesses are given in nanometers. (b) Conductance-bias curves under different magnetic configurations measured at $T = 0.07T_c$. The conductance is normalized so that $G(V = 7\ \text{mV}) = 1$ when $\mu_0 H = 0$. (c) The temperature dependence of the zero-bias conductance measured with a current bias $I_{\text{bias}} = \pm 0.5$ nA with $\mu_0 H = 0$, showing a superconducting critical temperature of 4.7 K, indicated by the dashed line. The decrease in conductance below T_c corresponds to the opening of a pseudogap in the conductance due to superconductivity.

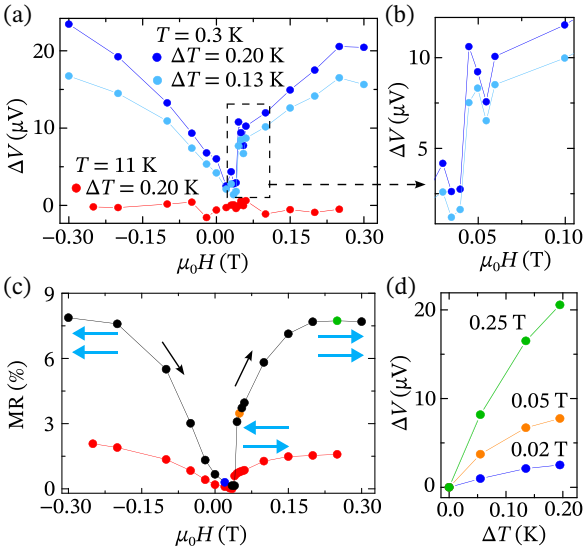

FIG. 2. The thermoelectric response of an F/S/F junction as a function of the upward swept applied in-plane (IP) magnetic field at $T = 0.3$ K and two different evaluated ΔT values. For comparison, a much smaller thermoelectric response observed above the critical temperature (at $T = 11$ K) is also shown. (b) An enlargement of the low-field region in (a), where an abrupt transition from the AP to the P state takes place. (c) Typical magnetoresistance (MR) curves versus the IP magnetic field at a bias of $V = 5$ mV at $T = 0.3$ K and 11 K. The blue arrows show the relative magnetic alignment of the ferromagnetic (F) electrodes, while the black arrow shows the direction of variation of the magnetic field. (d) The dependence of the TE response on the evaluated temperature difference between the F electrodes, measured at different IP magnetic states as indicated by the colored points in (c).

thin films grown in ultrahigh-vacuum conditions [35]. The steeper decrease in conductance at biases less than the superconducting gap and below T_c is due to the reduced density of states of vanadium at the Fermi level in the superconducting state. An alternative method to determine the superconducting critical temperature, which provides similar results, is related to the detection of the emergence of superconducting quasiparticle interference effects in conductance as a function of temperature [33].

In order to perform thermoelectric response measurements, we induce temperature gradients across the junctions by controlling the power dissipated by a light-emitting diode (LED) placed above them. This creates an inward heat flux on the top surface of the samples that can be tuned by biasing the LED at different voltages V_{LED}. We estimate the temperature profile and the total temperature difference ΔT across the heterostructure by solving the heat-diffusion equation in a one-dimensional (1D) model that approximates our samples (see the Supplemental Material [27]). We note that the estimated values of ΔT are in the order of 0.1–0.2 K, which indicates that the device could operate in a slightly nonlinear regime in measurements with a base temperature of 0.3 K. In the absence of an applied current ($I = 0$), the TE voltage ΔV generated under a given ΔT is obtained by subtracting the background voltage signal from the voltage measured under heating (for a discussion of the origin of the background TE signal, see the Supplemental Material [27]).

In Fig. 2(a), we present our main experimental observation: a substantial (over 10 times) change in ΔV between the AP and P alignments of the F electrodes. The Seebeck coefficient for the parallel alignment, calculated based on the estimated temperature gradients, reaches a value of approximately 100 μV/K (see the Supplemental Material [27]). The strong magnetic field dependence of the TE signal disappears above T_c. The data shown in Fig. 2 correspond to an upward sweep of the external in-plane magnetic field. Starting from the most negative H, as its magnitude decreases and the magnetic configuration transitions from the P to AP state, the TE signal changes relatively smoothly. In contrast, the transition from AP to P in the positive H branch leads to an abrupt increase in the TE response, accompanied by a subtle but reproducible "overshoot" effect, manifested as a peak followed by an immediate drop, shown in detail in Fig. 2(b).

The MR measurements performed during the TE experiments are shown in Fig. 2(c). The resistance R is measured at a bias of $V \sim 5$ mV under each value of the applied in-plane magnetic field H in thermal equilibrium before heating the junction with the LED. We define the

magnetic-field-dependent MR as

$$\mathrm{MR}(H) = \frac{R(H) - R_{\mathrm{min}}}{R_{\mathrm{min}}} \times 100\%. \quad (1)$$

Here, R_{min} is the minimum measured value of the resistance for a given base temperature and therefore corresponding to the magnetic state closest to a fully AP state.

Interestingly, we find that the resistance is higher in the P state than in the AP state, contrary to the seminal Fe/MgO/Fe-based heterojunctions [26,36,37]. We believe that the main reason for the negative MR in our F/S/F [ferromagnet/normal metal/ferromagnet (F/N/F) above T_c] junctions is that two Fe layers are separated by a relatively thick 40-nm vanadium film. Therefore, the simple picture explaining the conventional tunneling MR in Fe/MgO/Fe junctions may not be applicable to our structure. Importantly, early works on tunneling MR have demonstrated that the presence of different nonmagnetic spacers in between two F electrodes can alter not only its magnitude but also its sign [38]. More recently, the introduction of a vanadium film between Fe and MgO/Fe has been predicted to invert the MR sign [39].

We observe that the MR curve remains qualitatively similar above and below T_c, i.e., it decreases more smoothly in the P $\rightarrow$ AP transition in the negative H branch and increases more abruptly in the AP $\rightarrow$ P transition in the positive H branch. As we discuss below, based on micromagnetic simulations, the difference between the P $\rightarrow$ AP and AP $\rightarrow$ P transitions could be due to a rapid change in the relative magnetization configuration of the F electrodes during the AP $\rightarrow$ P transition due to the combined effects of macrospin rotation and domain-wall formation and displacement. The overall magnitude of the MR increases by approximately a factor of 3 in the superconducting state. We believe that the enhanced negative MR observed well below T_c could be attributed to a more effective spin-signal transfer between the two Fe electrodes through the 40-nm-thick V layer due to the generation of superconducting spin-triplet states [29,40].

In Fig. 2(d), we illustrate the TE response as a function of the temperature gradient at various fixed magnetic fields, color coded to correspond with the MR plot in Fig. 2(c), confirming a strong dependence of the TE response with the magnetic state of the junctions.

III. MICROMAGNETIC SIMULATIONS

Numerical simulations of the TE response require knowledge about the average angle between the magnetizations of the two ferromagnets enclosing the superconductor. This information has been obtained through micromagnetic simulations using the open-source software MuMax^3 [41]. At the same time, in order to mimic the experimental setup of Fig. 1(a), the system has been divided into three different regions. Region 1 models the soft 45-nm-thick Fe layer, region 2 the 10-nm-thick Fe layer and region 3 the 20-nm-thick Co layer, which together form the hard Fe/Co electrode (for simulation details, see the Supplemental Material [27]). To simulate a more realistic system, the presence of defects in the crystalline structure of the layers has been taken into account. A concentration of 25% for superficial and 10% for bulk defects has been considered (see the Supplemental Material [27]).

In our epitaxial Fe/MgO/V/MgO/Fe/Co vertically patterned junctions grown on MgO(001) substrate, the Fe(001) surface follows the cubic symmetry of the underlying MgO(001) lattice, leading to a dominant fourfold anisotropy with two easy axes along the two diagonals of the rectangular patterned junctions (along the MgO sides). This stabilizes two equivalent Fe (100) and Fe (010) magnetization directions marked (x) and (y) in Fig. 3(c), indicating both equivalent directions. As sketched in Fig. 1(a), Fe/Co consists of two separate layers, i.e., not intermixed Fe-Co. The first Fe(10-nm) layer interfacing MgO has a fourfold crystalline anisotropy, similarly to the soft Fe layer, and is hardened by the Co(20-nm) layer. The micromagnetic simulations have not assigned any in-plane or out-of-plane anisotropy to the Co layer to simulate magnetization reorientation and magnetoresistance. The possible out-of-plane anisotropy is irrelevant in our case, as the Co-layer thickness substantially exceeds 1–2 nm, where perpendicular magnetic anisotropy has been observed [42].

Moreover, owing to the presence of the low-field antiferromagnetic (AF) coupling between the two F layers, a negative exchange interaction has been introduced between regions 1 and 2 by means of a negative Ruderman-Kittel-Kasuya-Yosida (RKKY) coupling constant. Different RKKY constants from -0.5 mJ/m^2 to -2 mJ/m^2 have been considered. The simulations have been performed by varying the magnetic field starting from -0.5 T and continuing up to 0.5 T. The results for the angle difference $\Delta\theta(H)$ in Figs. 3(a) and 4(c) have been computed based on the macrospin of each region. In other words, the average magnetization vector for AF coupled regions 1 and 2 (see Fig. S5 in the Supplemental Material [27]) has been computed separately and then the angle between them has been calculated.

To calculate the MR, we have followed a simplified model [43] to approximate the magnetic-state-dependent conductance G for our junctions (for details, see the Supplemental Material [27]). We have simulated the MR using two approaches. The first one (Av.Angle) calculates the conductance as a function of the angle of the averaged magnetization in the two layers. The second approach divides the magnetic layers into a number of interfacial cells and then averages the conductance between each cell (a discretization size of $2.34 \times 2.34 \times 1.67$ nm^3 has been used; for the details, see the Supplemental Material

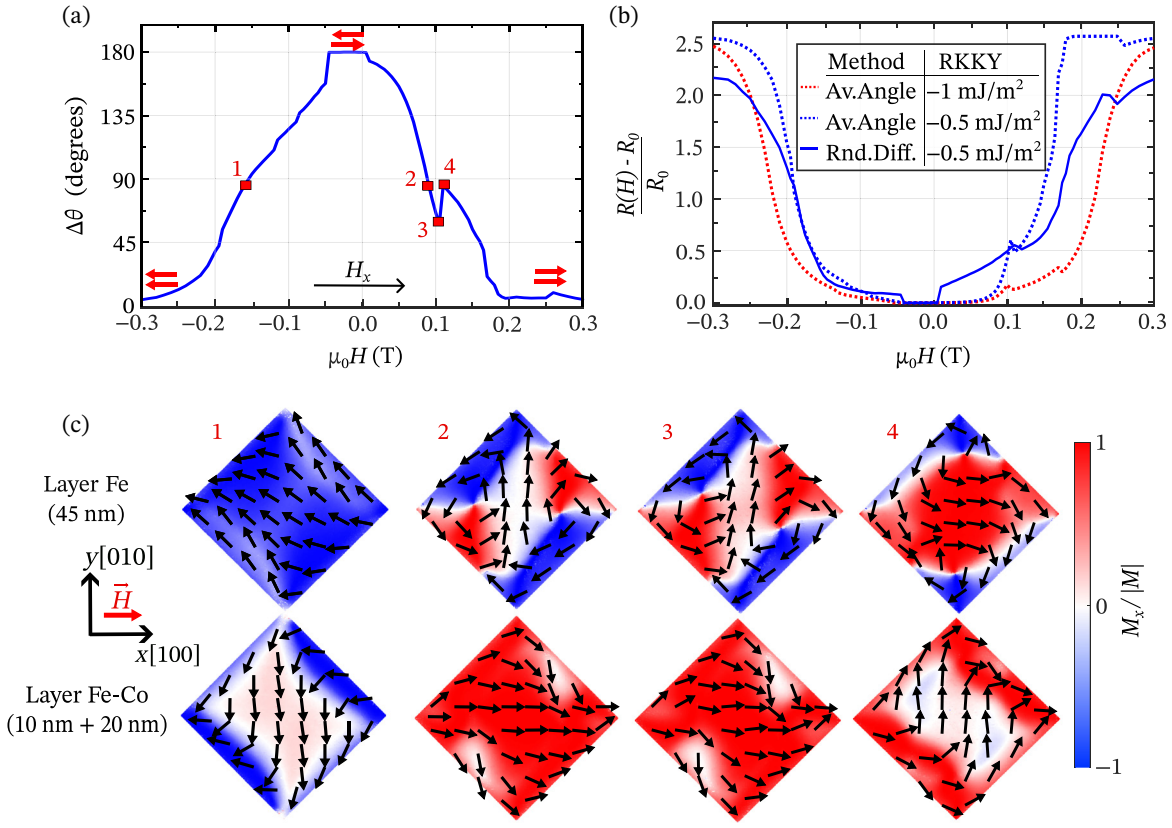

FIG. 3. (a) The angle difference between the macrospin of the two F regions for an antiferromagnetic (AF) coupling of RKKY $= -0.5$ mJ/m^2 (selected points highlighted with numbers), where RKKY is the Ruderman-Kittel-Kasuya-Yosida coupling constant. (b) The normalized magnetoresistance for two different couplings, calculated using two methods explained in the text, where R_0 is the resistance at $\mu_0 H = 0$. (c) The magnetization map for the interface of both F layers on the selected points in (a).

[27]) from the one electrode and a randomly chosen cell of the opposite electrode. Then, the electrodes have been interchanged and same procedure has been repeated. The second method (Rnd.Diff.) thus models the elastic impurity scattering of the electrons within the 40-nm-thick V layer separating the F electrodes. As one can observe in Fig. 3(b), using the lowest AF coupling value of RKKY $= -0.5$ mJ/m^2, the above-mentioned concentration of defects, and the Rnd.Diff. method, we obtain an MR curve that is qualitatively similar to the experimental measurements in Fig. 2(c). The magnetoresistance saturates above 0.3 T and the "overshoot" effect is reduced as in the MR experiments.

IV. THERMOELECTRICITY VIA NONEQUILIBRIUM QUASICLASSICAL THEORY

We use nonequilibrium Keldysh-Usadel Green's function theory [2,44] to numerically explore the setup in Fig. 1(a). We first provide an overview of the model used. A more technical description of the modeling is provided in the Supplemental Material [27]. Second, we combine the results from the quasiclassical simulations with the micromagnetic simulations to model how the thermoelectricity depends on the external magnetic field and we compare the result with the experimental data in Fig. 2(a).

The ferromagnets in Fig. 1(a) are treated as nonsuperconducting metallic reservoirs at temperatures T and $T + \Delta T$ for the soft (Fe) and hard (Fe-Co) ferromagnets, respectively. The voltages in the reservoirs are $\pm\Delta V/2$, respectively. The voltages are chosen such that the electrical current I through the system is zero. The interfaces to the superconductor are treated using spin-active tunneling interfaces with spin polarization p, tunneling conductance G_0, spin-mixing G_φ, and the average interface magnetization direction $\boldsymbol{m}$. The spin polarization filters incoming spins, while the spin mixing generates a spin splitting in the superconductor. The average interface magnetizations lie in the plane of the interfaces and the angle difference between the two interfaces is $\Delta\theta = \theta_2 - \theta_1$. This angle difference depends on the external magnetic field, as explained in the previous section. The superconductor is treated as a BCS [45] superconductor of length l. The model is illustrated in Fig. 4(a). We assume that the system is diffusive and we solve the Usadel equation [46] in the superconductor. This is done self-consistently for

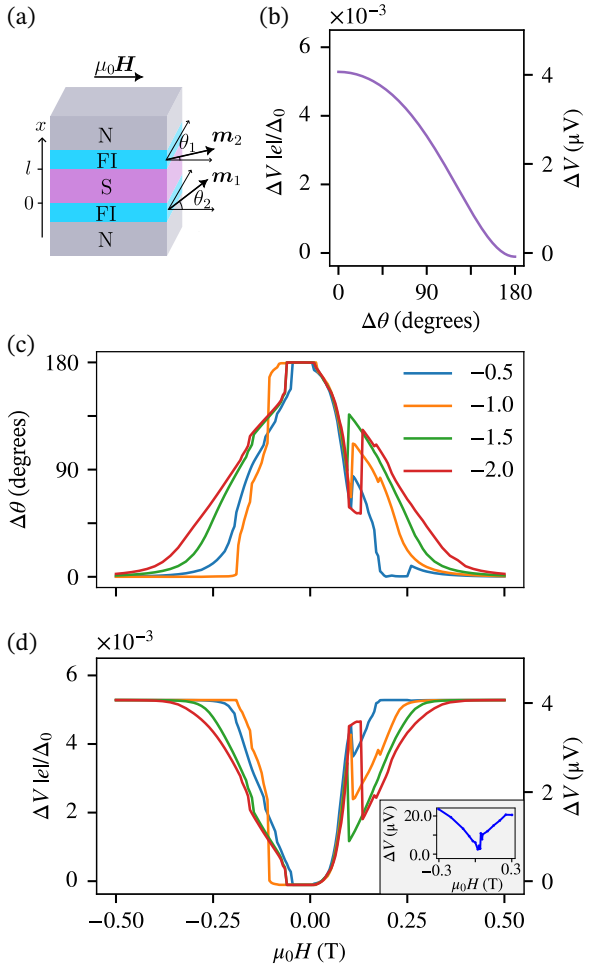

FIG. 4. (a) The model used in the numerical calculations. The superconductor (S) is sandwiched between two ferromagnets, modeled as nonsuperconducting (N) reservoirs with spin-active interfaces FI. The angle difference between the average in-plane magnetizations $\boldsymbol{m}_1$ and $\boldsymbol{m}_2$ of the interfaces is given by $\Delta\theta = \theta_2 - \theta_1$. The external magnetic field $\mu_0 \boldsymbol{H}$ affects $\boldsymbol{m}_1$ and $\boldsymbol{m}_2$ differently. (b) The induced thermovoltage ΔV as a function of the angle difference. Δ_0 is the bulk superconducting gap at zero temperature. (c) The simulated angle difference for an external magnetic field $\mu_0 H$ with four different RKKY couplings in units of mJ/m^2. (d) The thermovoltage as a function of the external magnetic field. For comparison, the inset shows the experimental results in Fig. 2(a) for $\Delta T = 0.2$ K.

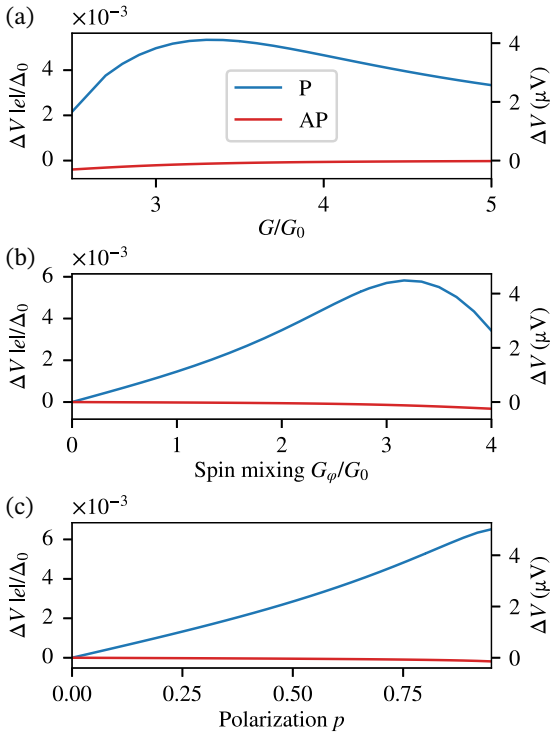

FIG. 5. The thermovoltage dependence on (a) the ratio of the bulk conductance to the interface conductance G/G_0, (b) the spin mixing G_φ, and (c) the interface polarization p in the parallel (P) and antiparallel (AP) configuration.

the superconducting order parameter. When the Usadel equation is solved, the current $I(\Delta V)$ is calculated. The thermovoltage is determined by solving $I(\Delta V) = 0$.

In the simulations, we use the values $G_0/G = 1/3.5$, $l = 1.5\xi$, and $p = 0.8$. Here, G is the normal-state bulk conductance and ξ is the diffusive coherence length of the superconductor. The spin-mixing angle is typically taken to be a fitting parameter and is set to $G_\varphi/G_0 = 2.75$. The temperature is set to $T = 0.057T_c^B$ and the temperature difference is $\Delta T = 0.038T_c^B$, where T_c^B is the bulk critical temperature of the superconductor. After solving the Usadel equation, we insert the numerical values $T_c^B = 5.3$ K and $\xi = 26$ nm [29,47], which yields $T = 0.3$ K, $\Delta T = 0.2$ K, and $l = 39$ nm. These are the values used to convert from dimensionless to numerical values in Figs. 4 and 5. We also use the BCS relation $\Delta_0/k_B T_c^B = 1.76$ between the bulk gap Δ_0 at zero temperature and the bulk critical temperature. The dependence of ΔV on $\Delta\theta$ is shown in Fig. 4(b). We note that with the chosen interface parameters, the quasiclassical simulations qualitatively reproduce the conductance curve in Fig. 1(c), although with a lower critical temperature of the superconducting film (not shown here).

A point requiring clarification is that while the temperature gradient and resulting thermovoltage are measured across the entire stack of materials in the experiment, the temperature gradient and thermovoltage are measured across the superconducting region in the theoretical modeling. However, this procedure is warranted for two reasons. As shown in the Supplemental Material [27], the simulations for the local temperature profile reveal that the vast majority of the temperature drop occurs precisely across the Fe/MgO/V interfaces and the superconductor, and not in the ferromagnets themselves. Moreover, the voltage drop across the junction has its primary contribution

coming from the interfaces between the ferromagnets and the superconductor due to the MgO barrier providing a high resistance. This matches the assumptions made in the theoretical model.

We use micromagnetic simulations for four different RKKY couplings, as shown in Fig. 4(c), to model the thermoelectric response to an applied magnetic field. The thermovoltage is presented in Fig. 4(d) as a function of the applied magnetic field and does qualitatively match the experimental data in the inset. The difference in magnitude of the thermovoltage between the simulations and measurements may be attributed to the restriction in quasiclassical theory regarding how the reservoirs are treated. Normal and ferromagnetic reservoirs are described by the same Green's function due to the requirement of a weak spin polarization in the quasiclassical approximation, unlike the strongly polarized ferromagnet Fe used in the experiment, and this likely reduces the numerically simulated value for ΔV. No such methodology restriction applies to the interfacial polarization in our treatment, however, which can model strongly polarized ferromagnetic interfaces [48].

V. DISCUSSION

Our experimental results demonstrate that the magnetic configuration of the superconducting spin valve changes the thermoelectric signal by more than an order of magnitude when switching from a parallel to an antiparallel state. After achieving a qualitative agreement between the experimental results and simulations of both the TE and MR effects, we conclude that the thermoelectric effects are highly sensitive to the collective domain rotation within the ferromagnetic layers, as shown in Fig. 3(c). At $H = 0$, due to the negative exchange interaction, the layers tend to align in an antiparallel configuration, resulting in the observed minima in resistance and TE signals. When an in-plane magnetic field is applied along one of the easy axes, the reorientation of the magnetization in the two ferromagnetic layers involves complex magnetic dynamics, including the formation of inner and edge domain walls, as illustrated in Fig. 3(c). Due to magnetocrystalline anisotropy, inner magnetic moments preferentially align toward the easy axes of the crystals, while the edge-located spins tend to minimize their normal component to reduce the stray field related energy contribution.

In Fig. 3, we also observe how the correlated rotation between the two ferromagnetic layers can induce an "overshoot" in the TE response [Fig. 2(a)]. The "overshoot" is seen as a sharp dip that occurs in the angle misalignment between the average magnetizations in Fig. 3(a). This correlated rotation of two antiferromagnetically coupled Fe layers from points 2 to 4 as marked in Fig. 3(a) is explained by the corresponding magnetization maps in Fig. 3(c). At point 3, one layer is mainly aligned along the x axis, while the other aligns along the y axis. At point 4, the alignment is interchanged. Following this transition, the layers continue to rotate toward a parallel alignment at high fields. This effect is observed in simulations and in the experiment only for AP $\rightarrow$ P transition, demonstrating the asymmetry between the P $\rightarrow$ AP and AP $\rightarrow$ P transitions.

The mechanism behind the thermoelectric effect was originally proposed in Refs. [14,15] and is described in detail in Ref. [25]. The effect relies on two properties of the structure. First, the superconducting density of states must be spin split. Second, the interfaces must filter the spins such that the density of states available for the thermally excited electrons and holes is asymmetric around the Fermi energy.

The thermoelectric effect is optimized when there is a large gap and spin splitting in the superconductor and the interface polarization is high. For the parameter sets in Fig. 4, the gap value is approximately 75% of the bulk value Δ_0 for all angle configurations of the interfaces. If the interface conductance is good, corresponding to low G/G_0, the gap is suppressed due to the inverse proximity effect. This is seen in the P configuration in Fig. 5(a). As the interface conductance decreases, the gap value and thus the thermovoltage increases. By reducing the interface conductance further, the superconductor becomes more isolated from the reservoirs and the transport across the superconductor is reduced. The spin mixing G_φ induces the spin splitting in the superconductor and the thermovoltage dependence on the spin mixing is shown in Fig. 5(b). When G_φ is zero, there is no spin splitting, while when G_φ is high, the spin splitting is large and superconductivity is destroyed. The optimal G/G_0 and G_φ values also depend on the length of the superconductor. A longer superconductor can withstand a higher interface conductance and spin mixing, thus increasing the thermovoltage. Moreover, sandwiching the superconductor in between the ferromagnets in the F/S/F structure increases the Seebeck coefficient compared to the superconductor/ferromagnet/ferromagnet (S/F/F) in Ref. [26], due to the increased spin splitting in the superconductor. In Fig. 5(c), we show that the thermovoltage increases with increasing interface polarization. This provides a way to optimize the thermoelectric effect. As seen in Fig. 5, the thermovoltage in the AP configuration is significantly smaller in magnitude than in the P configuration. This is because the average spin splitting in the AP configuration is smaller than in the P configuration.

Finally, we note that the large Seebeck coefficient in the P configuration remains large and more than an order of magnitude greater than in the AP configuration as the base temperature is increased, meaning that the effect is robust against an increase in temperature (see the Supplemental Material [27]). These theoretical predictions will be tested and verified in forthcoming experiments currently in preparation.

VI. CONCLUSIONS

We report the experimental observation of a large superconducting thermoelectric spin-valve effect that meets a number of key criteria required for cryogenic thermoelectric applications: (i) we use commercially available materials with high spin polarization, which are easily grown; (ii) there is a considerable thermoelectric effect, with a Seebeck coefficient exceeding 100 μV/K; and (iii) there is a large change in the thermoelectric response—greater than a factor of 10—when switching the device from AP to P alignment. The micromagnetic simulations and theoretical modeling based on the nonequilibrium Keldysh-Usadel Green's function formalism are consistent with both the thermoelectric and magnetoresistance results. As real cryogenic quantum systems are expected to operate under thermal gradients, integrating low-temperature Peltier elements into quantum computers could significantly enhance their performance. One promising future application of F/S/F-based devices is the recovery of heat inevitably generated during quantum error correction [21]. This is particularly relevant since most current quantum computers use qubits based on superconducting hybrid structures.

VII. METHODS

A more detailed explanation of the matters treated in this section is provided in the Supplemental Material [27].

A. Sample growth and experimental procedure

The F/S/F junctions studied in this work have been grown by molecular-beam epitaxy (MBE) and lithographed into 20×20 μm^2 lateral size samples. Both the MR and TE response measurements highlighted in Fig. 2 have been performed at temperatures of 0.3 K and 11 K, since these temperatures can be sustained in the cryogenic system (Janis He^3 cryostat) without the use of external heaters, minimizing extrinsic thermal gradients. The TE voltage ΔV results from subtracting the background-voltage signal from the voltage measured under heating at zero current bias. Different temperature gradients are induced by controlling the power dissipated by the LED by tuning its voltage bias V_{LED}. In MR measurements performed at thermal equilibrium, the voltage is measured at bias currents of $I = \pm 10$ nA and the resistance is calculated as $R = V/(2|I|)$. This current bias yields a voltage of approximately 5 mV.

B. Modeling of the temperature profile

In order to estimate the total temperature difference ΔT across the junction when heated under different V_{LED}, we solve the heat-diffusion equation in a 1D model of our junctions. We impose an inward heat flux q on one of the edges to account for the LED heating. The value of q is estimated by taking into account the power dissipated by the LED ($I_{\mathrm{LED}} \times V_{\mathrm{LED}}$) and its directionality through the radiation pattern provided by the manufacturer, the distance between the LED and the sample, and the contact area of the junctions that can absorb heat. The other edge of the system is fixed at a given temperature. We use the calculated values of ΔT to estimate the Seebeck coefficient under different magnetic fields, base temperatures, and temperature gradients.

C. Micromagnetic simulations

The relative angle between the ferromagnetic layers is calculated using micromagnetic simulations performed in MuMax^3 [41]. We simulate a 3D model of the magnetic layers our junctions with matching vertical dimensions. A phenomenological antiferromagnetic coupling is set between the two Fe layers of the system to reproduce the behavior under applied in-plane magnetic fields inferred from the MR measurements in Fig. 2(c). Superficial and bulk defects are implemented by lowering the saturation magnetization and adding disorder to the local magnetocrystalline anisotropy, respectively. The calculated MR displayed in Fig. 3(b) is obtained by using the Slonczewski formula [43] with a sign change to account for the negative MR induced by the presence of the V layers in between the two F electrodes.

D. Thermoelectricity via nonequilibirum quasiclassical theory

We use nonequilibrium Keldysh-Usadel Green's function theory [2,44,46] to model the thermoelectric effect in the F/S/F structure numerically. The ferromagnets are treated as nonsuperconducting metallic reservoirs with spin-active interfaces. We calculate the quasiclassical Green's function in the superconducting layer numerically by solving the Usadel equation self-consistently for the superconducting order parameter and find the voltage ΔV such that the charge current through the system disappears. The thermovoltage ΔV depends on the external magnetic field through the relative angle of the average interface magnetizations.

ACKNOWLEDGMENTS

The work in Madrid was supported by the Spanish Ministry of Science, Innovation and Universities (MICIU) (Grants No. PID2021-124585NB-C32, No. TED2021-130196B-C22, and No. PID2024-155399NB-I00). F.G.A. also acknowledges financial support from MICIU through the María de Maeztu Program for Units of Excellence in R&D (Grant No. CEX2023-001316-M) and Grant No. TEC-2024/TEC-380 (Mag4TIC-CM) projects. The work in Trondheim was supported by the Research Council of Norway through Grant No. 323766 and its Centres of Excellence funding scheme Grant No. 262633 "QuSpin." Support from Sigma2—the National Infrastructure

for High Performance Computing and Data Storage in Norway, Project No. NN9577K, is acknowledged.

DATA AVAILABILITY

All data available from corresponding authors by request and downloaded [49].

[1] G. Benenti, G. Casati, K. Saito, and R. S. Whitney, Fundamental aspects of steady-state conversion of heat to work at the nanoscale, Phys. Rep. **694**, 1 (2017).

[2] F. S. Bergeret, M. Silaev, P. Virtanen, and T. T. Heikkilä, Colloquium: Nonequilibrium effects in superconductors with a spin-splitting field, Rev. Mod. Phys. **90**, 041001 (2018).

[3] F. G. Aliev, V. V. Kozyrkov, V. V. Moshchalkov, R. V. Scolozdra, and K. Durcewski, Narrow band in the intermetallic compounds MNiSn (M = Ti, Zr, Hf), Zeit. Phys. Cond. Mat. **80**, 353 (1990).

[4] A. Ojha, R. K. Sabat, and S. Bathula, Advancement in half-Heusler thermoelectric materials and strategies to enhance the thermoelectric performance, Mater. Sci. Semicond. Process. **171**, 107996 (2024).

[5] T. M. Tritt, Thermoelectric phenomena, materials, and applications, Ann. Rev. Mat. Res. **41**, 433 (2011).

[6] J. Wei, L. Yang, Z. Ma, P. Song, M. Zhang, J. Ma, F. Yang, and X. Wang, Review of current high-ZT thermoelectric materials, J. Mater. Sci. **55**, 12642 (2020).

[7] Z. Soleimani, S. Zoras, B. Ceranic, S. Shahzad, and Y. Cui, A review on recent developments of thermoelectric materials for room-temperature applications, Sustainable Energy Technol. Assess. **37**, 100604 (2020).

[8] X.-L. Shi, J. Zou, and Z.-G. Chen, Advanced thermoelectric design: From materials and structures to devices, Chem. Rev. **120**, 7399 (2020).

[9] S. Irfan, Z. Yan, and S. Bashir Khan, Advancements in thermoelectric materials: A comprehensive review, Mater. Sci. Energy Technol. **7**, 349 (2024).

[10] J. Feng, J. Li, and R. Liu, Low-temperature thermoelectric materials and applications, Nano Energy **126**, 109651 (2024).

[11] S. R. Harutyunyan, V. H. Vardanyan, A. S. Kuzanyan, V. R. Nikoghosyan, S. Kunii, K. S. Wood, and A. M. Gulian, Thermoelectric cooling at cryogenic temperatures, Appl. Phys. Lett. **83**, 2142 (2003).

[12] J. T. Muhonen, M. Meschke, and J. P. Pekola, Micrometre-scale refrigerators, Rep. Progr. Phys. **75**, 046501 (2012).

[13] T. Heikkilä, M. Silaev, M. Virtanen, and F. S. Bergeret, Thermal, electric and spin transport in superconductor/ferromagnetic-insulator structures, Prog. Surf. Sci. **94**, 100540 (2019).

[14] P. Machon, M. Eschrig, and W. Belzig, Nonlocal thermoelectric effects and nonlocal onsager relations in a three-terminal proximity-coupled superconductor-ferromagnet device, Phys. Rev. Lett. **110**, 047002 (2013).

[15] A. Ozaeta, P. Virtanen, F. S. Bergeret, and T. T. Heikkilä, Predicted very large thermoelectric effect in ferromagnet-superconductor junctions in the presence of a spin-splitting magnetic field, Phys. Rev. Lett. **112**, 057001 (2014).

[16] S. Kolenda, M. J. Wolf, and D. Beckmann, Observation of thermoelectric currents in high-field superconductor-ferromagnet tunnel junctions, Phys. Rev. Lett. **116**, 097001 (2016).

[17] P. O. Sukhachov, E. W. Hodt, and J. Linder, Thermoelectric effect in altermagnet-superconductor junctions, Phys. Rev. B **110**, 094508 (2024).

[18] G. Marchegiani, A. Braggio, and F. Giazotto, Nonlinear thermoelectricity with electron-hole symmetric systems, Phys. Rev. Lett. **124**, 106801 (2020).

[19] G. Germanese, F. Paolucci, G. Marchegiani, A. Braggio, and F. Giazotto, Bipolar thermoelectric Josephson engine, Nat. Nanotechnol. **17**, 1084 (2022).

[20] F. Meng, J. Xu, X. Liu, and O. Dahlsten, Quantum harvester enables energy transfer without randomness transfer or dissipation, ArXiv:2406.08054.

[21] M. Bilokur, S. Gopalakrishnan, and S. Majidy, Thermodynamic limitations on fault-tolerant quantum computing, ArXiv:2411.12805.

[22] T. T. Heikkilä, R. Ojajärvi, I. J. Maasilta, E. Strambini, F. Giazotto, and F. S. Bergeret, Thermoelectric radiation detector based on superconductor-ferromagnet systems, Phys. Rev. Appl. **10**, 034053 (2018).

[23] A. Rajapaksha, S. D. Gunapala, and M. Premaratne, Enhanced thermal rectification in coupled qutrit-qubit quantum thermal diode, APL Quantum **1**, 046123 (2024).

[24] C. I. L. de Araujo, P. Virtanen, M. Spies, C. Gonzlaez-Orellana, M. I. Kerschbaumer, C. Rogero, T. T. Heikkilä, F. Giazotto, and E. Strambini, Superconducting spintronic heat engine, Nat. Commun. **15**, 4823 (2024).

[25] J. A. Ouassou, C. González-Ruano, D. Caso, F. G. Aliev, and J. Linder, Complete magnetic control over the superconducting thermoelectric effect, Phys. Rev. B **106**, 094514 (2022).

[26] C. González-Ruano, D. Caso, J. A. Ouassou, C. Tiusan, Y. Lu, J. Linder, and F. G. Aliev, Observation of magnetic state dependent thermoelectricity in superconducting spin valves, Phys. Rev. Lett. **130**, 237001 (2023).

[27] See the Supplemental Material at http://link.aps.org/supplemental/10.1103/xbgg-gttc for additional details on the experimental characterization of the samples, modeling of the temperature profile, micromagnetic simulations, quasiclassical theory, and the temperature dependence of the thermoelectric effect. The Supplemental Material also includes Refs. [50–66].

[28] I. Martínez, C. Tiusan, M. Hehn, M. Chshiev, and F. G. Aliev, Symmetry broken spin reorientation transition in epitaxial MgO/Fe/MgO layers with competing anisotropies, Sci. Rep. **8**, 9463 (2018).

[29] C. González-Ruano, L. G. Johnsen, D. Caso, C. Tiusan, M. Hehn, N. Banerjee, J. Linder, and F. G. Aliev, Superconductivity-induced change in magnetic anisotropy in epitaxial ferromagnet-superconductor hybrids with spin-orbit interaction, Phys. Rev. B **102**, 020405 (2020).

[30] B. Kochelaev, L. Tagirov, and M. Khusainov, Spatial dispersion of spin susceptibility of conduction electrons in a superconductor, Zh. Eksp. Teor. Fiz. **76**, 578 (1979).

[31] M. Khusainov, Multicritical points in the phase diagrams of layered ferromagnet-superconductor structures, Zh. Eksp. Teor. Fiz. **109**, 524 (1996).

[32] A. Di Bernardo, S. Komori, G. Livanas, G. Divitini, P. Gentile, M. Cuoco, and J. W. A. Robinson, Nodal superconducting exchange coupling, Nat. Mater. **18**, 1194 (2019).

[33] P. Tuero, C. González-Ruano, Y. Lu, C. Tiusan, and F. G. Aliev, Spin texture and spin-orbit coupling contributions in spin-triplet superconductivity, Phys. Rev. B **110**, 094504 (2024).

[34] J. M. Rowell and W. L. McMillan, Electron interference in a normal metal induced by superconducting contracts, Phys. Rev. Lett. **16**, 453 (1966).

[35] N. E. Alekseevskii, V. M. Sakosarenko, K. Blüthner, and H.-J. Köhler, Superconducting properties of vanadium films, Phys. Status Solidi (a) **34**, 541 (1976).

[36] S. S. P. Parkin, C. Kaiser, A. Panchula, P. M. Rice, B. Hughes, M. Samant, and S.-H. Yang, Giant tunneling magnetoresistance at room temperature with MgO (100) tunnel barriers, Nat. Mater. **3**, 862 (2004).

[37] S. Yuasa, T. Nagahama, A. Fukushima, Y. Suzuki, and K. Ando, Giant room-temperature magnetoresistance in single-crystal Fe/MgO/Fe magnetic tunnel junctions, Nat. Mater. **3**, 868 (2004).

[38] J. M. De Teresa, A. Barthélémy, A. Fert, J. P. Contour, F. Montaigne, and P. Seneor, Role of metal-oxide interface in determining the spin polarization of magnetic tunnel junctions, Science **286**, 507 (1999).

[39] X. Feng, O. Bengone, M. Alouani, I. Rungger, and S. Sanvito, Interface and transport properties of Fe/V/MgO/Fe and Fe/V/Fe/MgO/Fe magnetic tunneling junctions, Phys. Rev. B **79**, 214432 (2009).

[40] I. Martínez, P. Högl, C. González-Ruano, J. P. Cascales, C. Tiusan, Y. Lu, M. Hehn, A. Matos-Abiague, J. Fabian, I. Žutić, and F. G. Aliev, Interfacial spin-orbit coupling: A platform for superconducting spintronics, Phys. Rev. Appl. **13**, 014030 (2020).

[41] A. Vansteenkiste, J. Leliaert, M. Dvornik, M. Helsen, F. García-Sánchez, and B. Van Waeyenberge, The design and verification of MuMax3, AIP Adv. **4**, 107133 (2014).

[42] B. Dieny and M. Chshiev, Perpendicular magnetic anisotropy at transition metal/oxide interfaces and applications, Rev. Mod. Phys. **89**, 025008 (2017).

[43] J. C. Slonczewski, Conductance and exchange coupling of two ferromagnets separated by a tunneling barrier, Phys. Rev. B **39**, 6995 (1989).

[44] W. Belzig, F. K. Wilhelm, C. Bruder, G. Schön, and A. D. Zaikin, Quasiclassical Green's function approach to mesoscopic superconductivity, Superlattices Microstruct. **25**, 1251 (1999).

[45] J. Bardeen, L. N. Cooper, and J. R. Schrieffer, Theory of superconductivity, Phys. Rev. **108**, 1175 (1957).

[46] K. D. Usadel, Generalized diffusion equation for superconducting alloys, Phys. Rev. Lett. **25**, 507 (1970).

[47] C. González-Ruano Iriarte, Ph.D. thesis, Doctorate School in Condensed Matter Physics, Nanoscience and Biophysics, Universidad Autónoma de Madrid, 2023, https://repositorio.uam.es/handle/10486/711139.

[48] M. Eschrig, A. Cottet, W. Belzig, and J. Linder, General boundary conditions for quasiclassical theory of superconductivity in the diffusive limit: Application to strongly spin-polarized systems, New J. Phys. **17**, 083037 (2015).

[49] http://webs.fmc.uam.es/magnetrans.group/.

[50] C. Tiusan, F. Greullet, M. Hehn, F. Montaigne, S. Andrieu, and A. Schuhl, Spin tunnelling phenomena in single-crystal magnetic tunnel junction systems, J. Phys.: Condens. Matter **19**, 165201 (2007).

[51] C. R. Anoop, R. K. Singh, R. R. Kumar, M. Jayalakshmi, T. Antony Prabhu, K. Thomas Tharian, and S. V. S. Narayana Murty, A review on steels for cryogenic applications, Mater. Perform. Charact. **10**, 16 (2021).

[52] J. W. Gardner and A. C. Anderson, Effect of neutron irradiation on the low-temperature specific heat and thermal conductivity of magnesium oxide, Phys. Rev. B **23**, 1988 (1981).

[53] B. K. Chakal'skii, N. A. Red'ko, S. S. Shalyt, and V. M. Azhazha, Thermal conductivity of pure vanadium in normal, superconducting, and mixed states, Sov. Phys.—JETP **48**, 665 (1978).

[54] K. Balcerek, R. Wawryk, Cz. Marucha, J. Rafalowicz, and L. Krajczyk, Thermal conductivity and electrical resistivity of pure polycrystalline cobalt in the temperature range 2.5–30 K, Int. J. Thermophys. **17**, 1475 (1996).

[55] W. H. Butler, X.-G. Zhang, T. C. Schulthess, and J. M. MacLaren, Spin-dependent tunneling conductance of Fe|MgO|Fe sandwiches, Phys. Rev. B **63**, 054416 (2001).

[56] C. D. Graham, Magnetocrystalline anisotropy constants of iron at room temperature and below, Phys. Rev. **112**, 1117 (1958).

[57] L. P. Gorkov, On the energy spectrum of superconductors, Sov. Phys.—JETP **34**, 505 (1958).

[58] W. Belzig, F. K. Wilhelm, C. Bruder, G. Schön, and A. D. Zaikin, Quasiclassical Green's function approach to mesoscopic superconductivity, Superlatt. Microstruct. **25**, 1251 (1999).

[59] V. Chandrasekhar, *Superconductivity: Conventional and Unconventional Superconductors* (Springer-Verlag, Berlin, 2008), p. 279, chapter 8.

[60] G. Eilenberger, Transformation of Gorkov's equation for type II superconductors into transport-like equations, Z. Phys. **214**, 195 (1968).

[61] N. Schopohl and K. Maki, Quasiparticle spectrum around a vortex line in a *d*-wave superconductor, Phys. Rev. B **52**, 490 (1995).

[62] A. Konstandin, J. Kopu, and M. Eschrig, Superconducting proximity effect through a magnetic domain wall, Phys. Rev. B **72**, 140501(R) (2005).

[63] J. A. Ouassou, T. D. Vethaak, and J. Linder, Voltage-induced thin-film superconductivity in high magnetic fields, Phys. Rev. B **98**, 144509 (2018).

[64] N. M. Chtchelkatchev, T. I. Baturina, A. Glatz, and V. M. Vinokur, *Physical Properties of Nanosystems: Synchronized Andreev Transmission in Chains of SNS Junctions* (Springer, Yalta, 2009), p. 87, chapter 7.

[65] H. Shimada, K. Miyawaki, A. Hagiwara, K. Takeda, and Y. Mizugaki, Characterization of superconducting single-electron transistors with small Al/AlO_x/V Josephson junctions, Supercond. Sci. Technol. **27**, 115015 (2014).

[66] N. Ligato, G. Marchegiani, P. Virtanen, E. Strambini, and F. Giazotto, High operating temperature in V-based superconducting quantum interference proximity transistors, Sci. Rep. **7**, 8810 (2017).